On the role of barotropic versus baroclinic dynamics in generating a Taylor Cap at Maud Rise, Weddell Sea

Birte Gülk^{a,b}, Fabien Roquet^a, David Ferreira^c, Alberto C. Naveira Garabato^d

^a Department of Marine Science, University of Gothenburg, Sweden

^b Sorbonne Université, CNRS, IRD, MNHN, Laboratoire d'Océanographie et du Climat:

Expérimentations et Approches Numériques, LOCEAN/IPSL, F-75005 Paris, France

^c Department of Meteorology, University of Reading, Reading, U.K.

Orresponding author: Birte Gülk, birte.gulk@locean.ipsl.fr

^d Ocean and Earth Science, University of Southampton, Southampton, U.K.

ABSTRACT: A Taylor Cap originates from the flow's impingement on a seamount and subsequent formation of a quasi-stagnant volume above it, which isolates water properties and weakens the 11 stratification around it. Our focus is the Taylor Cap at Maud Rise, Weddell Sea, as this region is 12 prone to open-ocean polynyas. While previous studies have mainly examined the Cap's formation in a barotropic ocean, little attention has been paid to the role of baroclinic conditions, which are more 14 relevant to the real world. We study the behavior of a Taylor Cap in response to ambient stratification 15 and inflow conditions in an idealized model set up. Our investigation explores scenarios ranging from a barotropic set up to a simplified, quasi-realistic stratification associated with thermal wind. In the stratified cases, we determine the relative roles of the barotropic (depth-independent) and the 18 baroclinic (depth-dependent) flows, and investigate the local response of stratification. Our results show that the Taylor Cap is primarily generated by the deep barotropic flow, and that the baroclinic 20 component only forms a Taylor Cap if the velocity at the depth of the seamount is sufficiently 21 large. The baroclinic flow is, however, more effective at producing a doming of isopycnals over the 22 seamount. The limited ability of Maud Rise in trapping water masses stems from the Rise's large fractional height. Lastly, we show that higher inflow velocities lead to a shoaling of isopycnals and reduction of upper-ocean stratification over the seamount, with implications for the potential local onset of deep convection.

1. Introduction

48

55

The behavior of Taylor Caps, quasi-stagnant volumes above topographic obstacles with isolated 28 properties, can be important in ventilating and preconditioning the water column for deep convection (Ou 1991; Alverson and Owens 1996). One location where this is glaringly manifested 30 is Maud Rise, a seamount in the Weddell Sea, known for its occasional hosting of open-ocean 31 polynyas. Polynyas are openings in the sea-ice cover during the winter season. Several processes are thought to be significant for the formation of the polynya at Maud Rise. These processes can 33 be atmospheric (Francis et al. 2019), coupled oceanic-atmospheric (Campbell et al. 2019; Jena et al. 2019), and oceanic. The oceanic processes can be subdivided into vertical and convective instabilities (Gülk et al. 2024; McPhee 2003) and flow-topography interactions (Narayanan et al. 36 2024; Kurtakoti et al. 2018). The flow-topography interaction processes are enabled by the 37 impingement of the Weddell Gyre onto Maud Rise. The Weddell Gyre flows onto Maud Rise 38 and forms a northern and a weaker southern jets passing around the Rise (Schröder and Fahrbach 1999; Leach et al. 2011). The difference in the strength of the jets at the flanks of Maud Rise stems from the topography to the south of the Rise, which partially blocks the flow. The jets at the 41 flanks of Maud Rise can lead to eddy formation and upwelling of warmer deep waters, opening the polynya (Holland 2001; Cheon and Gordon 2019). Further, the jets flowing around Maud Rise 43 result in the emergence of a Taylor Cap (Gordon 1982; Muench et al. 2001; De Steur et al. 2007). 44 It has been reported that, before polynya openings, the properties of the Taylor Cap nearly vanish, and warmer, saltier waters flow over the Rise (Gülk et al. 2023; Narayanan et al. 2024), suggesting 46 an important role of Taylor Cap dynamics in favoring polynyas. 47

The theory of Taylor Caps is an extension of the theory of Taylor Columns, which was first described by Taylor (1923) and Proudman (1916) in the Taylor-Proudman theorem. In this 50 theorem, when a rotating, inviscid, barotropic flow moves across a topographic obstacle, a 51 stagnant cylinder, the so-called Taylor Column, is formed on top of the obstacle. In the case of a stratified fluid, the Taylor Column was first referred to as Taylor cone by Hogg (1973), but is more 53 commonly termed Taylor Cap nowadays (Chapman and Haidvogel 1992).

Taylor Columns and Caps have been the subject of research from a fluid dynamics perspective 56 since the 1970s. Their behavior and response to various parameters have been studied in idealized 57 To allow for a comparison between the different studies, various non-dimensional 58 numbers are considered. The geometry of the domain and obstacle are described by the fractional height and aspect ratio. The fractional height h^* is the ratio between the obstacle height h and 60 the water depth of the domain H, $h^* = h/H$. The aspect ratio contextualises the dimensions via 61 H/L, where L is the half-width of the seamount. The dynamics of the experimental set-up are described by the Rossby number and Burger number. The Rossby number compares advection to Coriolis force by Ro = U/fL, with U as characteristic velocity, f as Coriolis parameter and L as characteristic length scale (e.g., half-width) of the seamount. The Burger number indicates if a system is dominated by rotation or by stratification, and is estimated as Bu = NH/fL, where N is 66 the mean buoyancy frequency of the experiment. 67

68

Hogg (1973) investigated a small topographic obstacle ($h^{\star} \ll 1$) interacting with a slow flow $(Ro \ll 1)$, which was horizontally uniform and had a baroclinic current in a linear stratification 70 He concluded that the obstacle's vertical influence depends on the stratification, 71 topographic configuration and upstream shear. A weak stratification ($Bu^2 \ll 1$) leads, with a certain size of the topographic obstacle, to the emergence of a Taylor Column; in a moderate stratification $(Bu^2 \simeq 1)$, a Taylor Cap emerges with any obstacle height. The height of the Taylor Cap is set by the strength of the stratification. James (1979) studied the requirements for nonlinear effects in the vicinity of an isolated hill with a barotropic fluid in a rotating system, and showed that those effects are dependent on the hill's height and the Ekman number, which 77 is defined as $E_k = \frac{v}{fH^2}$ with v as viscosity and H as vertical layer thickness. In that study it was shown that different types of Taylor Columns can occur, classified as "inertial" or "viscous" depending on the amount of viscous pumping induced by the imposed flow. We will return to this 80 important distinction in our final discussion, arguing that Maud Rise caps are in the viscous regime. 81

82

Ou (1991) identified dynamical regimes in a uniform, two-layer flow with a cylindrical obstacle, and determined in which regime ventilation of the lower layer is possible by varying the obstacle's height and the parameter space of stratification. In a simulation of a tall, isolated seamount in a steady, rotating, nearly inviscid, stratified flow, Chapman and Haidvogel (1992) found that the height, width and temporary trapping of water parcels of the Taylor Cap are dependent on the inflow and fractional height of the seamount. They tested a variety of fractional heights between $\lesssim 0.1$ and 0.9, Rossby numbers between 0.04 and $\gtrsim 0.2$, and Burger numbers of Bu = 0 and Bu = 1. For seamounts with a fractional height of $h^* > 0.4$, permanent Taylor Caps only occurred with weak inflows, as stronger inflows trap water parcels only temporarily. Alverson and Owens (1996) studied the behavior of the Taylor Cap in a stratified domain with uniform surface cooling, in which a barotropic mean flow impinged on a Gaussian bump. They focused on a configuration with a Rossby number of 0.08, a fractional height of 0.5, and a Burger number of 1. Their work emphasised the interaction of the surface mixed layer with the Taylor Cap and the conditions needed to trigger deep convection. They showed that deep convection is strongly promoted if the Taylor Cap penetrates across the surface mixed layer base.

Some of these idealized studies connected their findings to the behavior of the Taylor Cap at Maud Rise. Ou (1991) identified the dynamical regime that is needed to ventilate the water column. For Maud Rise, the small baroclinic deformation radius compared to the large obstacle size, combined with cooling, weakens the stratification and ventilates the deeper layers. In his two-layer experiments, occurrence of the Taylor Column is expected in both layers, and can experience alterations from diabatic fluxes. Other studies used an idealized version of Maud Rise and increased complexity to study the effects of multiple layers, strength of the barotropic inflow, and bathymetry (De Steur et al. 2007). These authors showed that increasing the inflow velocity leads to a shoaling of isopycnals, and thus brings subsurface heat closer to the surface.

Most modelling studies contributing to the knowledge of Taylor Columns / Caps have hitherto focused on a barotropic inflow condition. Even Hogg (1973), who considered baroclinic flows, did not treat the case of finite depth obstacle such as Maud Rise. Here, we aim to determine the relative roles of baroclinic versus barotropic dynamics in generating Taylor Caps at Maud Rise, and to describe the resulting Taylor Cap properties. We define the barotropic component of the flow as the depth-independent flow equal to the bottom flow. In contrast, we define the baroclinic component as the depth-dependent residual flow with zero velocity at the bottom level. In other words, the

barotropic flow is set by the bottom velocity and all deviations from the bottom flow are included in the baroclinic flow, as is customary in the observational community (Peña-Molino et al. 2014).

Note that this definition is different from the one often used in theoretical studies decomposing the flow into vertical modes of variability, where the barotropic component corresponds to the depth-averaged flow, and the baroclinic component is the residual, e.g. Wunsch (1997). In practice, we do not expect our results to be sensitive to this choice of definition, as the bottom layer is always much deeper than the upper layer, making the baroclinic flow surface-intensified in any case.

To investigate the relative roles of baroclinic and barotropic flows, we use an idealised set up 124 with a Gaussian topographic bump with dimensions similar to Maud Rise. We start with the case 125 of a homogeneous layer and a barotropic inflow. Then, we add stepwise complexity in the form of 126 additional temperature layers, a linear meridional temperature gradient, an e-folding temperature 127 profile, and a realistic stratification based on a global reanalysis product. Some of the set-ups 128 contain a baroclinic flow as well as a barotropic component. Using this approach, we investigate the impacts of the various inflow conditions, and determine their role in generating a Taylor Cap. 130 Further, we explore the response of stratification to variations in the barotropic inflow in a sensitivity 131 experiment.

2. Methods

123

We use the MITgcm (Marshall et al. 1997) ocean model to investigate the characteristics of the Taylor Cap. A total horizontal domain size of 1500 km x 1000 km is set up with a horizontal 135 resolution of $\Delta x = \Delta y = 25 \,\mathrm{km}$ in Cartesian coordinates. The domain is centered at 65.4° S on a 136 β -plane with a Coriolis parameter of $f = -1.3 \cdot 10^{-4} \text{s}^{-1}$ and $\beta = 1.3 \cdot 10^{-11} \text{m}^{-1} \text{s}^{-1}$. The domain is bounded by a solid wall at the northern and southern boundaries. The maximum depth is 5 000 138 m, divided in 100 equal vertical levels with a $\Delta z = 50$ m. We use an idealized Gaussian bump 139 as bathymetry, based on the diameter and height of Maud Rise (Figure 1). The Gaussian bump, 140 placed at the center of the domain, is surrounded by a flat bottom of 5000 m depth and rises to a depth of 2 000 m (i.e., h=3000 m). The half-width of the Gaussian bump is L=100 km. In 142 general, the imposed flow is westward, to simulate the westward flow of the Weddell Gyre at 143 Maud Rise. All experiments are 3 650 days long, with 30-day output, except for the barotropic

case which is only 375 days long due to the fast adjustment timescale. The last 30-day output is used for further analysis.

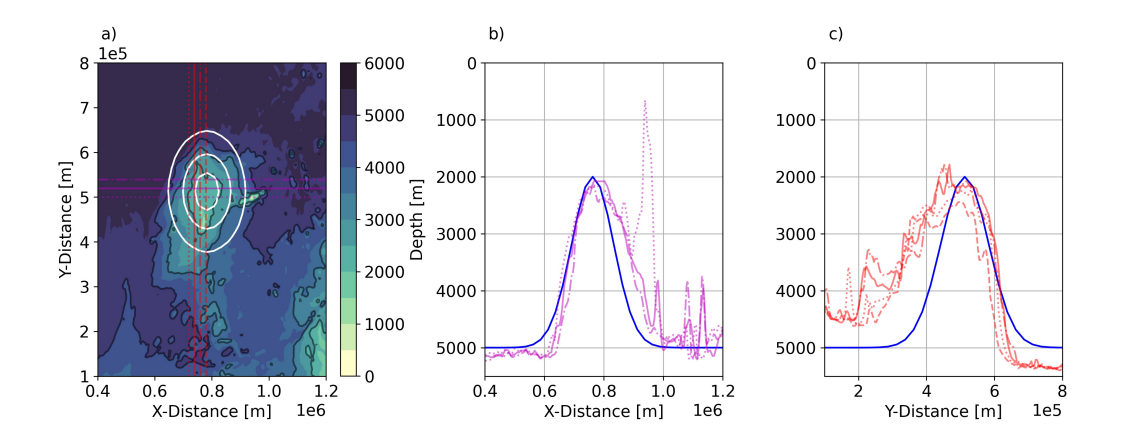


Fig. 1. a) Comparison of Maud Rise bathymetry (background) with 2 500, 3 500 and 4 500 m isobaths (grey lines) and the same isobaths of the idealized Gaussian bump (white circles). b,c) The blue line shows the cross section of the center of the idealized Gaussian bump. Magenta / red lines refer to the cross section of Maud Rise indicated in a).

We use a linear equation of state,

$$\rho = \rho_0 \left[1 - \alpha_0 \left(\theta - \theta_0 \right) \right], \tag{1}$$

with $\rho_0 = 1035 \text{ kg m}^{-3}$, $\alpha_0 = 1 \cdot 10^{-4} \text{ K}^{-1}$, and θ as temperature. α_0 corresponds to a salinity of $S = 34 \text{ gkg}^{-1}$ and $\theta = 4^{\circ}\text{C}$ at surface pressure. The values of α_0 and ρ_0 are also used as parameters in the model configuration. Due to the use of a linear equation of state, the stratification is controlled by temperature, with a constant salinity throughout the domain at $S=30 \text{ gkg}^{-1}$. The simulation is run without eddy parameterization, despite being at a non-eddying resolution. Sensitivity tests with eddy parameterization have shown only minor differences, mostly in modulating the stratification around the Rise. However, these differences did not change the conclusions of this study. Our model set up does not contain an atmosphere or sea-ice, and we focus solely on the oceanic response to stratification and inflow conditions.

All in all, we investigate several cases of stratification (Figure 2) and inflow conditions:

- A) one layer with a barotropic inflow of $u_{bt} = -0.1 \,\mathrm{m \, s^{-1}}$;
- B) 20 equally-thick temperature layers with temperature decreasing by $\Delta\theta = -0.05^{\circ}$ C with depth, and a barotropic inflow of $u_{bt} = -0.1$ m s⁻¹;
- 167 C1) adding a linear meridional temperature gradient to case B ($\Delta T = 1.83$ °C between minimum and maximum temperatures in the domain), so that the meridional mean temperature remains the same as in case B. The inflow is a baroclinic component derived from the thermal wind balance (dashed white lines in Figure 2b);
- 171 C2) same as C1, but the inflow has an additional barotropic component, starting with $u_{bt} = -0.1 \,\mathrm{m \ s^{-1}}$ for comparison with A and B. To test the impact of the barotropic inflow on the upward displacement of isotherms, and the response of upper-ocean stratification in a stratified ocean scenario, case C2 is repeated with different velocities for the barotropic component: $u_{bt} = [-0.01, -0.02, -0.05, -0.08, -0.10, -0.12, -0.15, -0.18, -0.20, -0.25] \,\mathrm{m \ s^{-1}}$. This set of experiments is denoted C2[X], where X is the value of u_{bt} ;
- D1) e-folding scale of 1 000 m for temperature stratification with a meridional gradient ($\Delta T = 9^{\circ}$ C).

 The inflow is a baroclinic component derived from the thermal wind balance;
- D2) same as D1, but the inflow has an additional barotropic component; $(u_{bt} = -0.1 \,\mathrm{m\,s^{-1}})$;
- E1) a temperature section based on a realistic density transect from a global reanalysis product,

 GLORYS12 (Lellouche et al. 2021), upstream of Maud Rise. The baroclinic flow is derived

 from the thermal wind balance;
- E2) same as E1, but employing a barotropic and a baroclinic flows. The mean of the total inflow is the same as the mean of the extracted GLORYS12 u-velocity section.
- For the almost realistic cases E1 and E2, we extract a meridional section of temperature, salinity and u-velocity at 15.5°E from GLORYS12 (Lellouche et al. 2021). In these sections, ridges are interpolated, then the resulting values are interpolated onto the model grid. Remaining bathymetric grid cells are filled with neighboring values in order to not induce a horizontal density gradient. Using the interpolated temperature and salinity sections, ρ is computed. The resulting density value is converted back into an equivalent temperature using a constant salinity of $S = 35 \,\mathrm{g\,kg^{-1}}$ (Figure 2d). From this equivalent temperature section, the density is derived using the linear

- equation of state, then the thermal wind balance is computed. The thermal wind represents the
- baroclinic flow u_{bc} . To derive the barotropic flow u_{bt} , we compute

$$u_{bt} = \langle u_{G12} - u_{bc} \rangle_{y,z},\tag{2}$$

where u_{G12} is the u-velocity of the GLORYS12 section after interpolation.

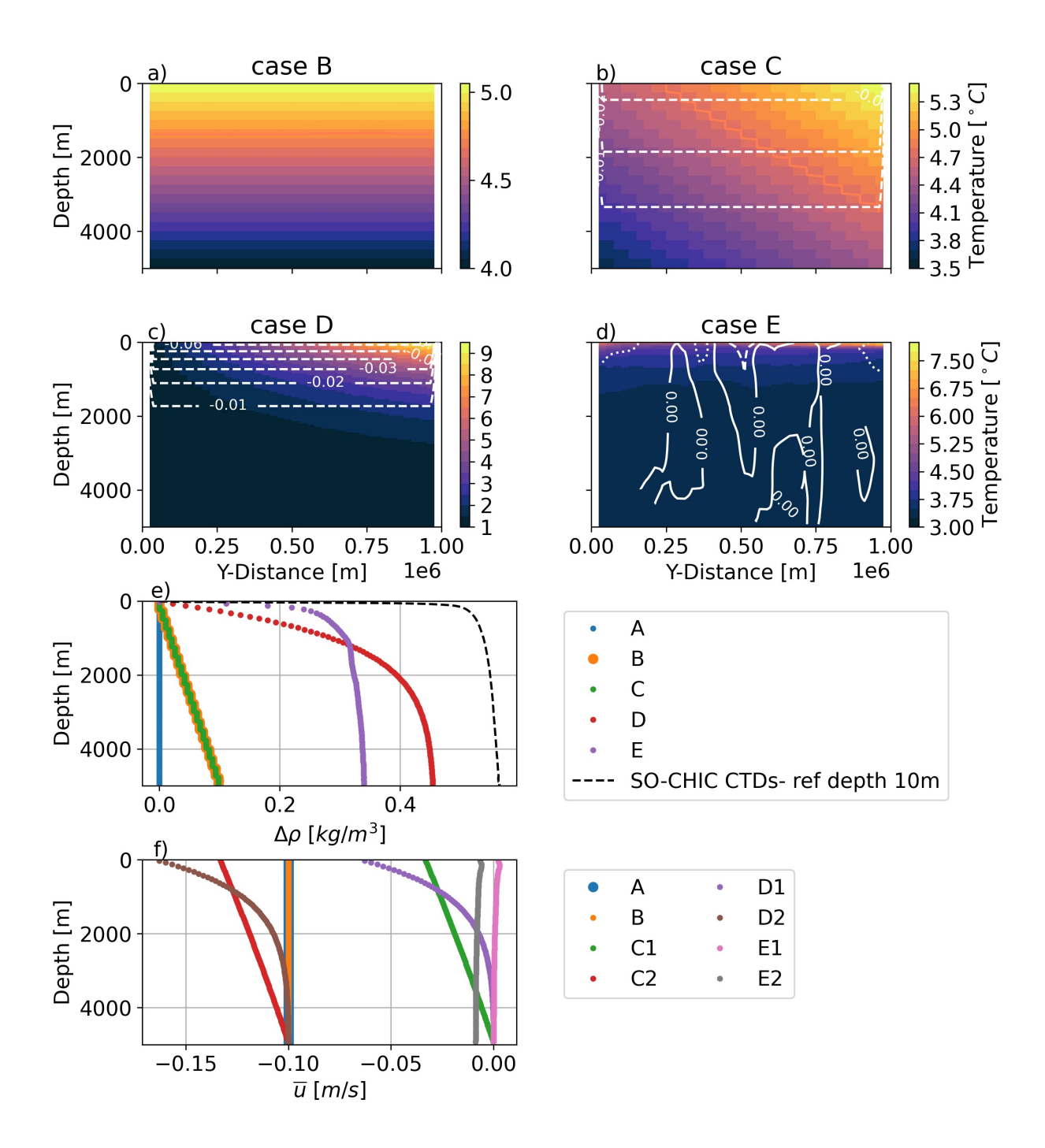


Fig. 2. a-d) Meridional temperature sections representing the initial conditions for cases B - E. White lines in b-d indicate the baroclinic velocities derived from the density, dashed lines indicate a negative velocity. e)
Horizontal-mean density anomaly with reference to the surface for all cases, and mean ρ anomaly from the SO-CHIC cruise in 2022 (Gülk et al. 2023) (black dashed line). f) Mean meridional u-velocity profile for the different cases.

All cases are investigated in terms of their differences in sea surface height (SSH), temperature structure, and upper-ocean density relative to the equilibrium state. Most of the experiments reach equilibrium by the end of the simulation; an exception is case D2, which shows minor variations in the SSH especially at the southern boundary of the domain.

To contextualise our model set-up in a theoretical framework, we compute the related non-dimensional numbers such as the Rossby number, fractional height, aspect ratio, Ekman number and Burger number. Throughout the different cases, the aspect ratio and fractional height are constant, with a fractional height of 0.6 and an aspect ratio of 0.05. The Rossby number varies slightly as it is dependent on the inflow u, yet $Ro \le 0.01$. The Ekman number is also constant throughout our cases and has a value of $E_k = 2$. The Burger number is dependent on the initial stratification N, and therefore varies between the cases. We determine N from the initial set up based on the linear equation of state, and compute the mean of the domain excluding the outermost grid point. As we do not have a stratification in case A, the Burger number is Bu = 0. For cases B and C, the Burger number is Bu = 0.37. For case D, a Burger number of Bu = 0.28 is determined, and Bu = 0.17 for case E.

This means that our set-ups encompass a wide range of dynamical regimes, providing a generalisation of studies found in the literature, including those described in Chapman and Haidvogel (1992); Alverson and Owens (1996); Ou (1991); Hogg (1973) and James (1979). This will facilitate further comparisons of our results with the existing literature, while exploring Taylor Cap regimes more systematically.

3. Results

224 a. Surface structure of the Taylor Cap

In this section, we analyze how increasing the complexity of the impinging flow (cases A-E2) affects the presence / absence and intensity of Taylor Columns and Caps by investigating how the SSH and its anomaly change between the cases (Figure 3). The SSH anomaly is defined as the SSH field after removing the SSH values from the zonal mean of the 200 km downstream

of the eastern boundary (Figure 3, pink box) from the SSH field. We define a Taylor Column as having a positive SSH anomaly on the northern flank and a separating barotropic flow along the 230 northern and southern flanks of the bump. In the barotropic case A (Figure 3a), a Taylor Column 231 is formed, with strong positive SSH anomaly over the center-north part of the bump, while in the southern part a depression in SSH is found. When stratification is added (case B), the SSH and 233 SSH anomaly fields are similar to those of case A, although the SSH anomaly is slightly weaker 234 by 5% constantly over several outputs. If the water column is forced only by the baroclinic inflow 235 component (case C1, Figure 3e), then the SSH field shows no strong meridional gradient, and the 236 SSH anomaly of the Taylor Cap is weaker than in the previous cases. This weakening results from 237 a slower inflow. If a barotropic component is added to the inflow condition (case C2[-0.10], Figure 238 3c), the SSH anomaly field of the Taylor Cap is increased compared to C1, but the maximum 239 anomaly is still weaker than those of cases A and B. The SSH anomaly in case C2[-0.10] is 240 reduced by 8% ($\sim 3\%$) compared to case A (B) constantly over several outputs. The more realistic 241 stratification in case D1 hints a separating barotropic flow, yet no Taylor Cap emerges in the SSH (Figure 3f). When combining the baroclinic component with a barotropic flow (case D2, 243 Figure 3d), the Taylor Cap's SSH anomaly intensifies again, although the anomaly is much weaker 244 than in cases A (by 41%), B and C2[-0.10]. In cases E1 and E2 (Figure 3g,h), employing a broadly realistic stratification, a Taylor Cap is formed only when barotropic and baroclinic inflows 246 are combined. The baroclinic inflow only (case E1) does not generate a Taylor Cap. The SSH 247 anomaly in cases E1 and E2 is weaker than in any previous case, a result of slower inflow velocities.

The set up of cases C1 and C2[-0.10] facilitates an approximate estimation of the relative contribution of barotropic and baroclinic flows to the SSH signal, by subtracting the SSH anomaly of case C1 from that of case C2[-0.10] (Figure 4). This decomposition shows that most of the SSH anomaly in the combined case originates from the barotropic component. The barotropic component in the combined case resembles that in case B, but is slightly weaker.

b. The impinging flow and barotropic vorticity

249

255

256

258

259

From the eight cases considered, a Taylor Cap emerges fully in six cases only, while in case D1 a

Cap is suggested in the barotropic velocity field and in case E1 no Cap occurs. To elucidate which

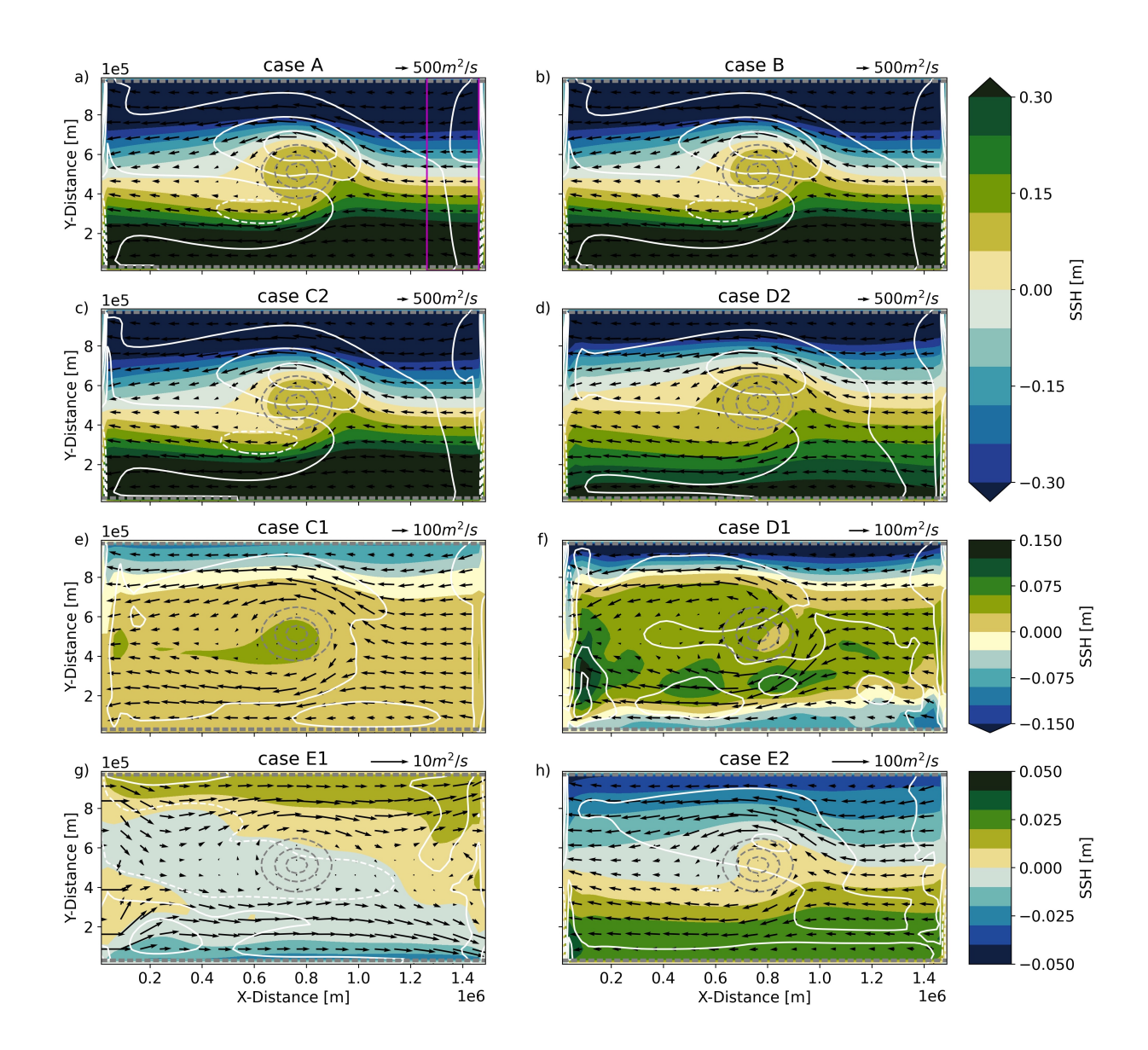


Fig. 3. SSH of the last output of the different cases. White solid (dashed) lines indicate a positive (negative) SSH anomaly with the zonal mean of the pink box removed. Arrows indicate the barotropic velocity of every third data point. Note different color scales for each row. Grey circles indicate 2 500, 3 500 and 4 500 m isobaths.

vertical level of the horizontal flow is most important for forming a Taylor Cap, we investigate velocity profiles upstream of the Gaussian bump ($\Delta x = 362.5 \,\mathrm{km}$, Figure 5c blue star). This position is chosen to be upstream of the separation of the vertically-integrated flow into a northern and a southern jets along the flanks of the Gaussian bump.

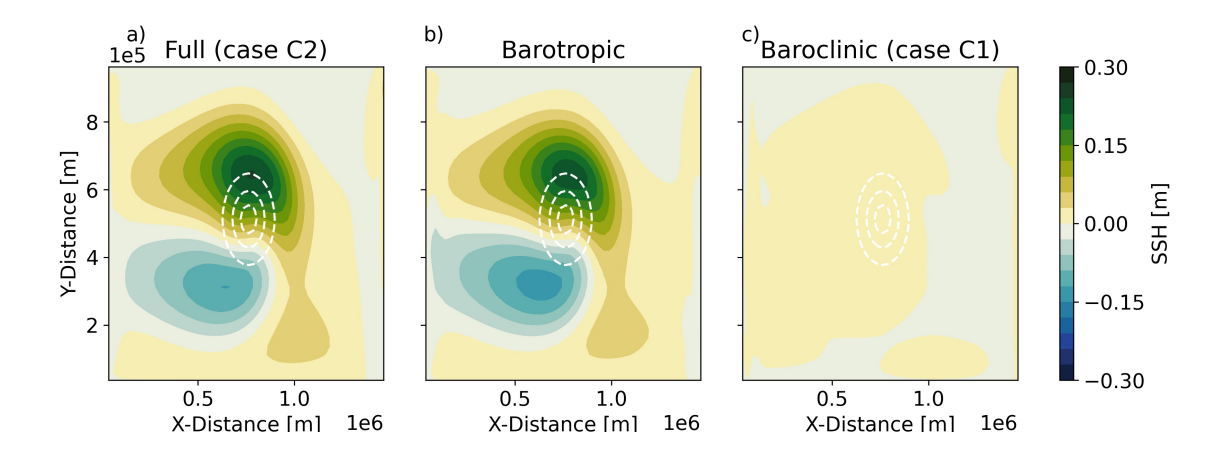


Fig. 4. Decomposition of the SSH anomaly of a) case C2[-0.10] into components associated with the b) barotropic and c) baroclinic flows (case C1).

268

269

270

271

272

274

275

277

278

279

280

281

282

284

285

In cases A, B and E2, almost no difference in the velocity profile between near-bottom and upper-ocean velocities is found (Figure 5a), but both velocities are different from 0 and a Taylor Cap is generated. In case E1, no flow is found below the uppermost 500 m, and no Taylor Cap emerges. The velocity profiles of C1 and C2[-0.10] resemble each other, with an offset due to the added barotropic component. The offset is reflected in the strength of the Taylor Cap signal in the SSH (Figure 3 c, e). More interesting are the velocity profiles of cases D1 and D2. These do not only differ by the offset of the barotropic component, but the velocity in D1 also decreases just below the maximum height of the Gaussian bump and reaches 0 m s⁻¹ at the bottom. Here, the Taylor Cap signal is only found in the barotropic velocity field and does not emerge in the SSH. In all cases with a Taylor Cap, we find a vertical mean u-velocity below the maximum height of the obstacle to be larger than 0 m s⁻¹. In case E1, this velocity is 0 m s⁻¹. In D1 the velocity does not reach zero, yet it is not strong enough to significantly interact with the bump and generate a Taylor Cap. Thus, one can conclude that the near-bottom velocity of the impinging flow is more important than the upper-ocean velocity (recall that cases C1 and D2, which have weaker velocities than D1 at 2000 m depth, do produce a Cap). In all cases in which a fully-developed Taylor Cap is found, the near-bottom velocity is similar to or higher than the upper-ocean velocity. This is also reflected in a comparison of the baroclinic u-velocity component, Δu , with the maximum SSH anomaly in the vicinity of the Gaussian bump from all runs, including the variations of case C2 (Figure 5b). Δu is the difference between the bottom and surface u-velocity values at the

same position as that of the velocity profiles in Figure 5a. With the same Δu , SSH anomalies of varying strength are found, indicating that the SSH anomaly is set by the near-bottom velocity (or, equivalently, the barotropic component of the flow).

We have shown that the impinging near-bottom velocity is important to form a Taylor Cap. This can be rationalized using barotropic potential vorticity (PV), which is defined as the curl of the vertically-integrated velocity (barotropic transport),

$$\zeta_{bt} = -\frac{\partial \int u dz}{\partial y} + \frac{\partial \int v dz}{\partial x}.$$
 (3)

In the cases where a Taylor Cap is generated, a positive vorticity is found at the bump's northern flank and a negative vorticity at the southern flank (Figure 5c,d). This pattern is similar in all cases with a Taylor Cap, with the strength of the pattern being dependent on the impinging barotropic flow. In case C1, where the barotropic flow is one fifth of the barotropic flow in case A, the resulting vorticity is also only one fifth of that in case A. In case C2[-0.10], the fastest impinging bottom velocities are found (Figure 5a), and the resulting barotropic vorticity is largest amongst all cases A-E2. The barotropic vorticity patterns vary in case D1, where a Taylor Cap is suggested, and in E1, where no Cap occurs. In case D1 (Figure 5e), a positive vorticity is found in the northern half of the bump, and a negative vorticity occurs on the southern side. This pattern is slightly different to the one of case A as a negative vorticity occurs in the center. In case E1 (Figure 5f), the vorticity patterns are opposite to those in any other case, as a result of the eastward impinging flow. This pattern mainly stems from the flow in the upper ocean, and does not generate a Taylor Cap.

Strikingly, we do not find an isolated patch of anomalous vorticity over the Rise in any of the simulated cases, contrasting with the usual expectation of a Taylor Column. This suggests that the Taylor Cap is only partially developed, and thus has a reduced ability to isolate water masses and store property anomalies. This is consistent with the results of Gülk et al. (2023), who found a 6-month residence time over the Rise. We will return to this point in the discussion.

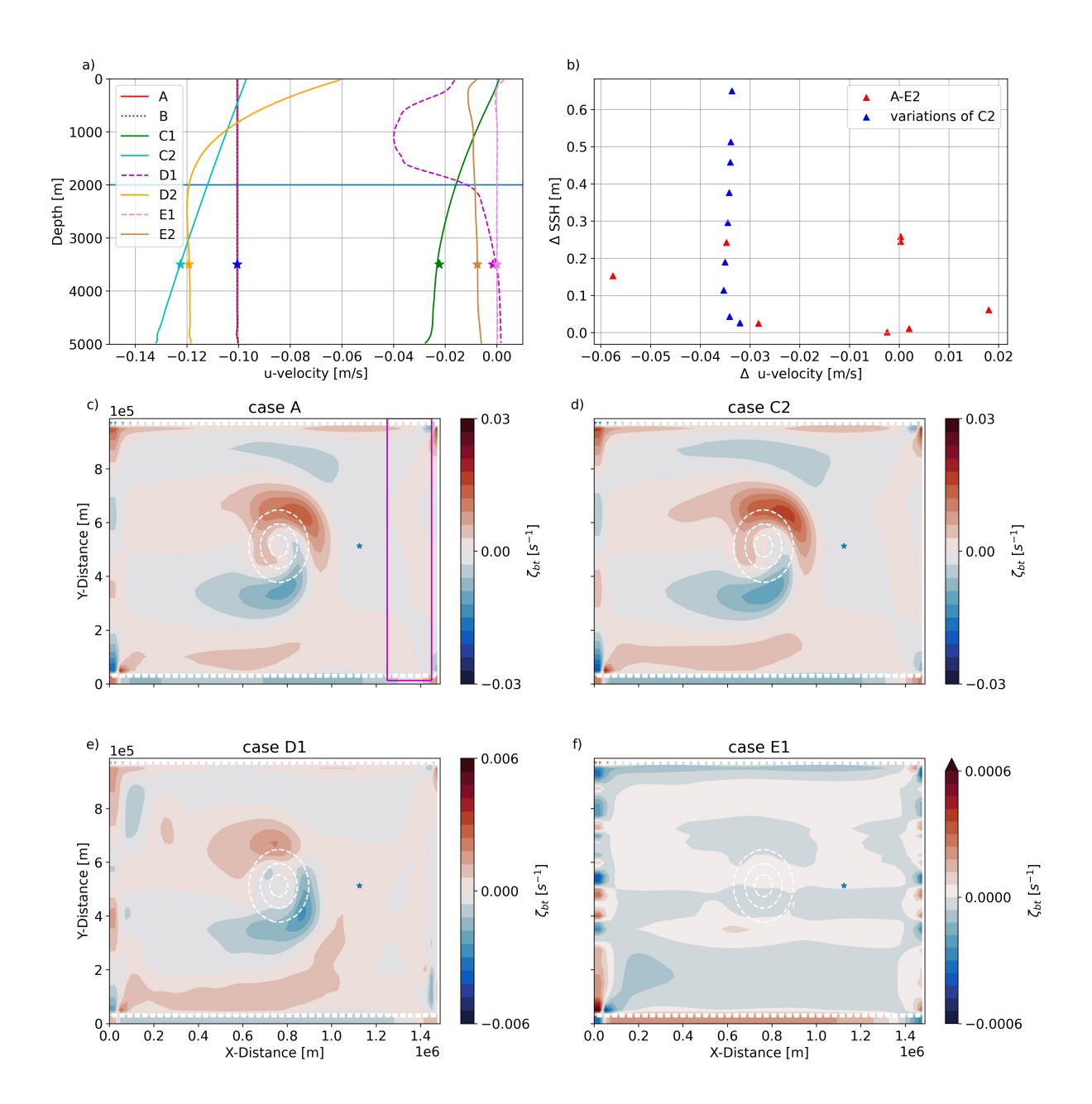


Fig. 5. a) u-velocity upstream of the Gaussian bump for the different cases. Dashed lines indicate the velocity profiles that did not lead to the emergence of a full Taylor Cap. The horizontal line at 2 000 m depth indicates the maximum height of the bump. The stars refer to the vertical mean velocity of the flow below the maximum height of the bump. b) baroclinic component Δu versus maximum SSH anomaly in the vicinity of the Gaussian bump. c-f) barotropic vorticity ζ_{bt} at the last output after removing the zonal mean of the pink box. The star indicates the location of the velocity profile in a) and b)

s c. Vertical structure of the Taylor Cap

Examining the surface signature of the Taylor Cap in the eight different cases highlights that a flow with a baroclinic component only can form a Cap if significant changes in the stratification extend to the bottom and introduce a bottom flow. Here, we investigate the vertical structure of temperature and vertical velocity along the zonal direction crossing the center of the Gaussian bump (Figure 6). In case A, only the vertical velocity is shown due to the absence of stratification (Figure 6a). The vertical velocity exhibits a strong upward signal when the flow impinges on the obstacle, followed by downwelling as far as the center of the bump. On the western side of the bump's center, a weak upward velocity is found, followed by downward flow on the lee side of the obstacle. The vertical velocity signal almost reaches the surface. In case B, isotherms are almost horizontal, and a small vertical upward displacement is found at the eastern side of the bump that decays by 500 m water depth. The vertical displacement is focused on the locations in which strong up- and downward velocities are found. The vertical velocities are comparable to case A, yet on the eastern side a second cell of up- and downwelling forms close to the center of the bump.

In case C1, the vertical displacement of isotherms at the eastern side is more pronounced, and above the bump a downward displacement of the isotherms is found with an accumulation of warm temperatures in the surface area above the center. Vertical velocities are weaker than in cases A or B, which stems from the slower impinging flow in case C1 (Figure 5a). In case C2[-0.10], the vertical displacement of isotherms reaches the surface and leads to outcropping of some isotherms. The vertical velocities are stronger than in case C1, and comparable to those in cases A and B as the impinging flow is of the same order (Figure 5a).

In case D1, isotherms are almost horizontal, and only minor vertical displacement is found. In the vertical velocity, only weak signals of up- and downwelling occur. In case D2, a minor vertical displacement is found, indicating a doming of the isotherms above the obstacle throughout the water column. When a barotropic component is added to the inflow, upwelling and downwelling near the obstacle increase. The stratification suppresses vertical flow into the uppermost 500 m. Here, cases B, C1 and C2[-0.10] show that the baroclinic component leads to an increase in vertical displacement of isotherms. The results of cases E1 and E2 show almost horizontal isotherms (not

shown) and vertical velocities that are lower by one order of magnitude compared to the previous cases. The up- and downwelling patterns occur only in E2. Vertical velocities are one order of magnitude smaller in cases E1 and E2, as is the impinging flow.

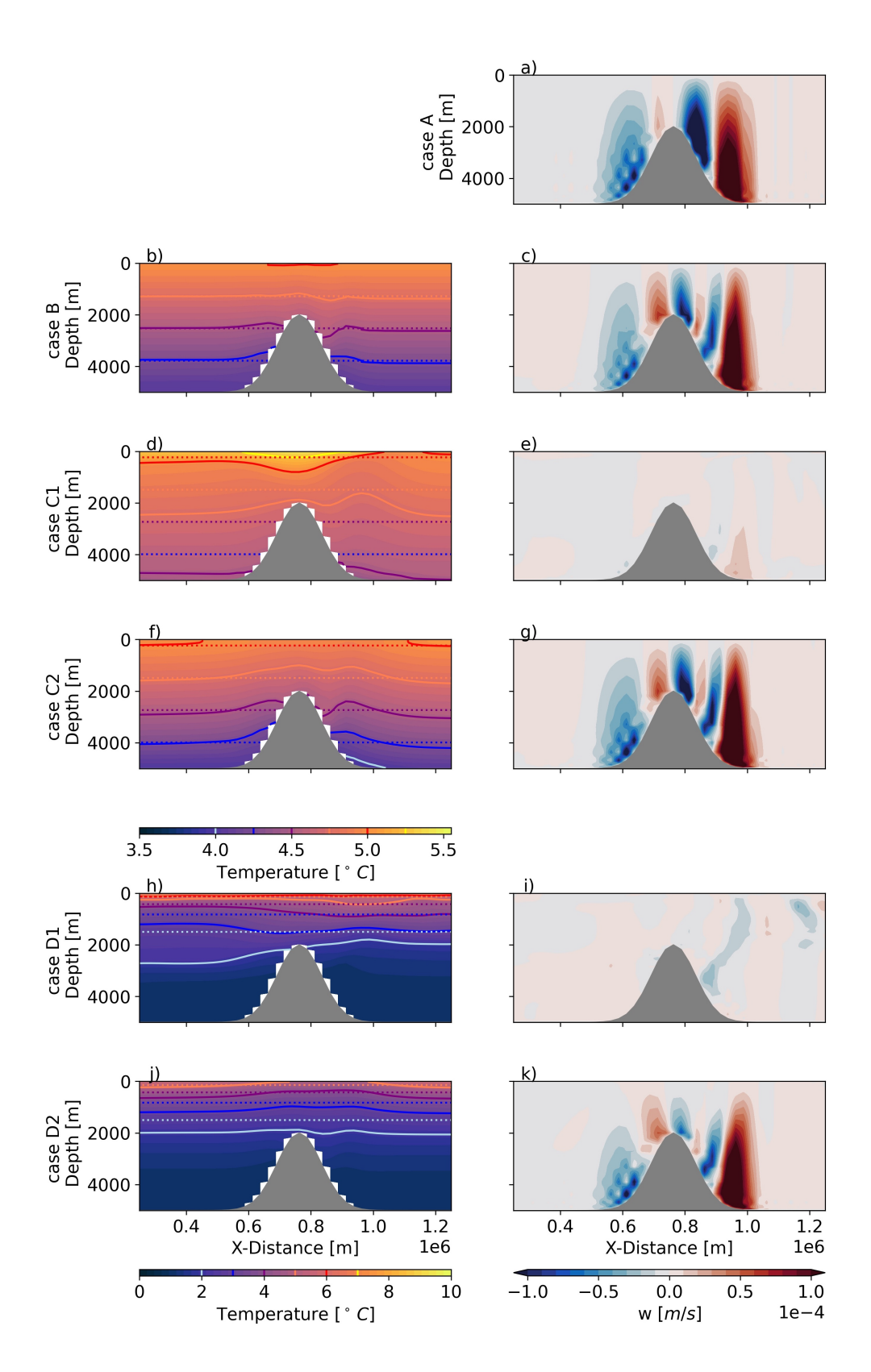


Fig. 6. Zonal temperature section across the center of the bump at the last output of the different cases (left column) and the corresponding sections of vertical velocity (right column). Colored lines refer to different isotherms as indicated on the colorbar; dotted lines denote the position of the isotherms at t=0.

Analyzing the eight cases reveals that the deep barotropic flow is the main contributor to the 356 generation of the Taylor Cap, but that the baroclinic component plays a non-negligible role in 357 modulating the Cap's strength within the water column. The isotherms' vertical displacement 358 reflects the up- and downwelling cells on the flanks of the Gaussian bump in all cases with a Taylor Cap (Figure 6), but the doming is not in proportion to the strength of up- and downwelling. 360 For example, case C1 shows greater doming of isotherms than cases B or C2[-0.10], yet the up-361 and downwelling cells are stronger in cases B and C2[-0.10]. It is also notable that in case B, 362 which has a horizontal stratification with no imposed baroclinic flow, a vertical displacement of 363 isotherms still occurs. Adding vertical shear from case B to case C1 shows that the isotherms' 364 doming is more pronounced, indicating that such doming is a response to both stratification and vertical shear. In fact, it would be hard to separate the two effects, as it is the sloping of the 366 stratification which creates a baroclinic flow. 367

d. Impact on stratification around the Taylor Cap

368

We investigate the upward displacement of isotherms and associated changes in stratification in response to varying the barotropic inflow component in case C2 (Figure 7). Recall that the baroclinic component, which is the same in all C2[X] simulations, is combined with different values for the barotropic component.

Using these runs, we focus on the vertical displacement of the 4.75° C-isotherm. This isotherm 375 lies at 1500 m depth in the initial state at the center of the Gaussian bump. First, we investigate the 376 spatial changes in the depth of the 4.75° C isotherm by computing the depth difference between the 377 final state and the zonal-temporal mean of the first 200 km downstream of the eastern boundary, to estimate the response to the different barotropic velocities (Figure 7a-d). With no barotropic 379 velocity component ($u_{bt} = 0 \,\mathrm{m \ s^{-1}}$, case C1, Figure 7a), the 4.75° C isotherm shows an upward 380 displacement upstream of the Gaussian bump and on the northern and eastern flanks, while in the south the isotherm deepens. With the addition of a barotropic component in the inflow, the 382 isotherm experiences a stronger upward displacement at the northern and eastern flanks, while the 383 deepening at the southern flank is further weakened. The upward displacement becomes stronger with larger barotropic components, while the weakening remains in the same range. In a last step,
we compare the isotherms' spatial patterns in three locations: the northern flank, the center of the
bump, and the southwestern flank (Figure 7d). The northern (southwestern) location is chosen
due to the deepening (flattening) introduced in the previous analysis (Figure 7a-c), and we aim
to connect this vertical displacement with the prescribed barotropic inflow component. In the
northern flank and the center, isotherms rise in proportion to the prescribed barotropic flow, while
on the southwestern flank the deepening is less sensitive to the barotropic velocity.

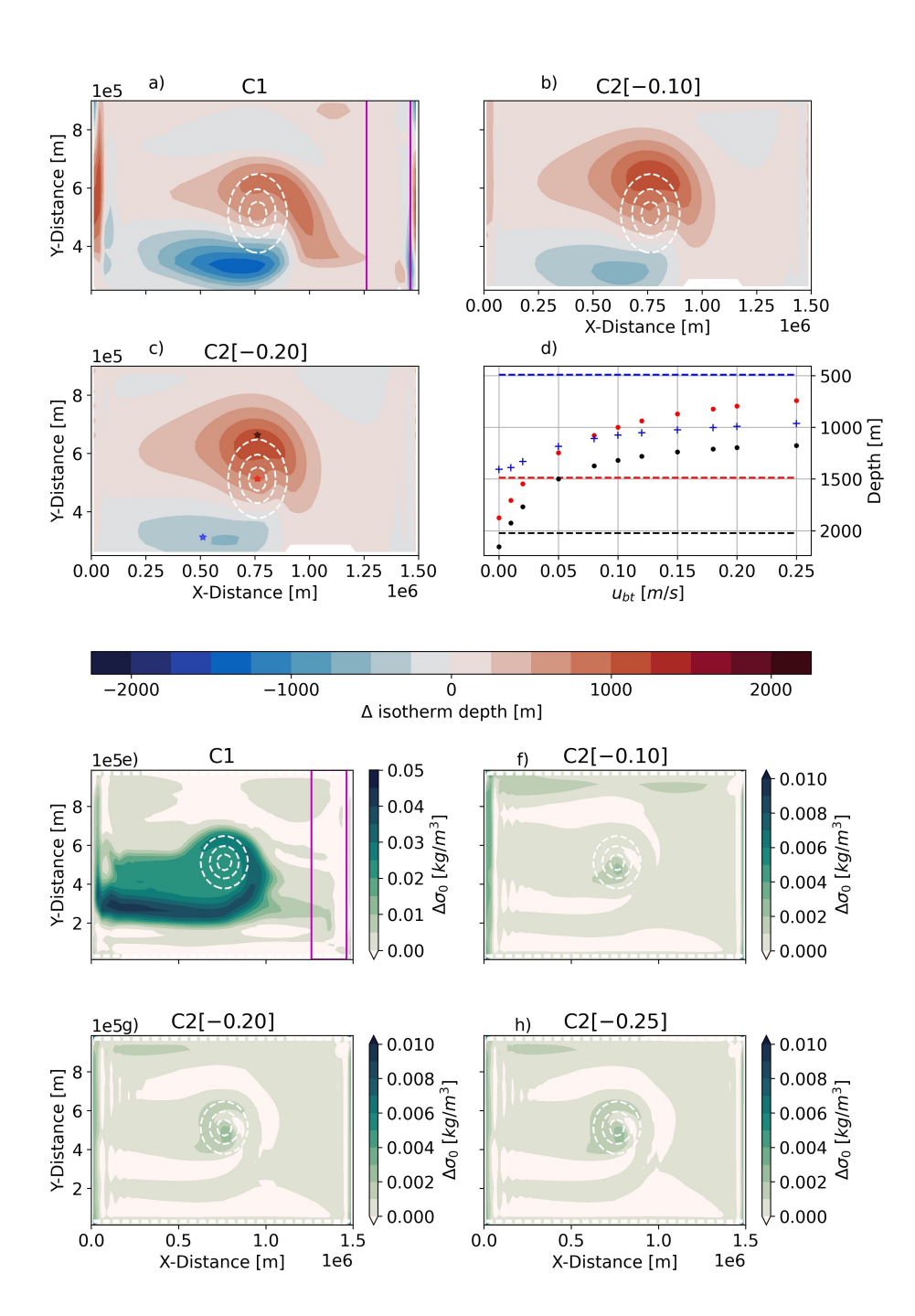


Fig. 7. a-c) Depth difference in the 4.75° C isotherm between the final states and the zonal-temporal mean of the pink box. White circles indicate 2 500, 3 500 and 4 500 m isobaths. d) Depth of the 4.75° C isotherm displacement for all sensitivity runs of case C2 as a function of the barotropic component in the inflow condition. Colors refer to the locations indicated in c), dashed lines denote the initial depth at that location. e-h) σ_0 difference between 525 m and 25 m depth at the final time step after removing the zonal-temporal mean of the pink box. White circles indicate 2 500, 3 500 and 4 500 m isobaths.

Previous tests highlight that stronger barotropic velocities bring subsurface waters closer to the 399 surface in regions where upwelling occurs, and lead to a westward displacement of this feature. To 400 understand how the upward displacement impacts changes in stratification, $\Delta \sigma_0$ is computed as the 401 density difference between 525 m and 25 m in the final state and removing the zonal-temporal mean of the first 200 km downstream of the eastern boundary (Figure 7 e-h). As the initial stratification 403 is identical in all runs, changes in $\Delta \sigma_0$ can be related to the inflow condition. This shows that with 404 higher barotropic velocities, the density in the upper ocean decreases locally in the vicinity of the Gaussian bump and downstream to the southwest of the bump. These simulations thus show that a sufficient barotropic velocity is necessary for the stratification in the vicinity of the bump to be 407 affected.

4. Discussion and Conclusions

423

We have studied the generation of Taylor Caps related to properties found at Maud Rise, 410 using idealized simulations by testing different stratification and inflow conditions that range from a purely barotropic ocean to a broadly realistic stratification. Our study demonstrated that 412 the generation of the Taylor Cap is associated with the near-bottom flow's impingement on the 413 topographic obstacle. The near-bottom flow is mainly set by the barotropic flow condition. The baroclinic condition only plays a role if a sufficiently strong horizontal flow at near-bottom depth is 415 generated, which may then interact with the Gaussian bump. In cases D1 (with an e-folding scale 416 stratification) and E1 (with a broadly realistic stratification), for which the density profiles are comparable to observations and the inflow only in thermal wind balance, the baroclinic component 418 did not introduce a sufficiently intense flow at depth to generate a Taylor Cap, even considering 419 that the e-folding scale of the density profile was deeper than in hydrographic data (Figure 2g, red 420 dots and dashed lines). This set of simulations also highlighted that the baroclinic component, 421 expressed both via stratification and vertical shear, is associated with a doming of isopycnals. 422

In the second set of experiments, we investigated the effect of an increased barotropic component in the inflow condition, and showed that higher velocities lead to an increased doming of isopycnals and a westward displacement of the Taylor Cap. This westward displacement due to a stronger inflow condition is in line with observations at Maud Rise (Muench et al. 2001). The increased

doming of isopycnals was documented by De Steur et al. (2007) and related to intensified barotropic velocities impinging on the bump. This increases the bottom pressure torque in the barotropic vorticity balance, which induces the vertical velocities on the upstream side of the bump. The doming brings subsurface heat closer to the surface, and can thus play an important role in releasing heat to the atmosphere, modulating sea-ice concentration in winter or air-sea fluxes. Further, we have shown that increased barotropic velocities may lead to a weakening of upper-ocean stratification, thus making the area more susceptible to deep convection.

To summarize the roles of barotropic and baroclinic flows regarding the Taylor Cap at Maud Rise, we find the Taylor Cap to be generated by the impinging barotropic flow. The velocity of the barotropic and baroclinic combined inflow is related to the shoaling of isopycnals and reduction of upper-ocean stratification. The baroclinic component is responsible for the doming of isopycnals, and therefore it can play a key role in the Taylor Cap's interaction with the mixed layer, which can lead to deep convection (Alverson and Owens 1996). As shown by Alverson and Owens (1996), a deepening of the mixed layer and a shoaling of the Taylor Cap are needed to trigger deep convection. To further investigate the role of baroclinic flow here, it would be necessary to include atmospheric and sea-ice fluxes in the model configuration, which is beyond the scope of our study.

We did not find simulated Taylor Caps to be associated with an isolated patch of anomalous vorticity over the Rise. This contrasts with the classical picture of a Taylor Column consisting of a patch of barotropic PV cancelling the effect of bottom topography changes on the PV. Here, we find instead a dipole of barotropic PV wrapping around the topographic obstacle. James (1979) illustrates different regimes of Taylor Caps, depending on the Rossby number and the relative fraction of depth of the topographic obstacle. For a small Rossby number and high topographic obstacle, he showed that bottom friction becomes important. He defines the non-dimensional number $S = \frac{h^*}{Ro}$, where Ro is the Rossby number, and h^* the fractional height of the bump. For O(1) values of S, an "inertial" regime emerges in line with the classical picture of a vorticity patch over the bump. However, for large values of S, the effect of bottom friction becomes large, leading to a "viscous" regime. The Taylor Cap properties generated in our idealized set-ups closely resemble those in this latter regime (see Figure 4 of James (1979)). This is consistent with the

fact that we have a modest Rossby number of $Ro \sim 0.01$ and a large fractional height of $h^{\star} \sim 0.6$, thus a number S = 60 around Maud Rise. This highlights the likely importance of bottom friction in controlling the structure of the Taylor Cap at Maud Rise, and the limited ability of the Cap in retaining water masses there (Gülk et al. 2023). Chapman and Haidvogel (1992) showed that Taylor Caps have the potential to trap water temporarily. They identified this potential to occur for fractional heights between 0.4 and 0.6, and Rossby numbers between 0.1 and 0.2 (their Figure 20). Yet in their study they focused on steady, stratified flows with a Burger number of 1. In our work, we show that temporary trapping of water can also occur for lower Rossby numbers in combination with smaller Burger numbers.

A potential limitation of the present work is that the horizontal resolution of 25 km used in our model simulations is rather coarse. This allowed us to explore the parameter space at reasonable computational cost, but puts into question the degree of realism of our simulations. It has been reported that Taylor Cap generation may be resolution-dependent, via the resolution's impact on the steepness of the topographic slope (Kurtakoti et al. 2018). Furthermore, Maud Rise is believed to be a region with eddy shedding at its flanks, based on both observations and realistic simulations (Leach et al. 2011; Holland 2001; Mohrmann et al. 2022; Gülk et al. 2023). Hallberg (2013) estimated that a horizontal resolution of 1/25° (~4 km) would be required to resolve the first baroclinic Rossby radius at Maud Rise, a resolution that exceeds what most global models can currently achieve (which typically employ a horizontal resolution of 1/12° or less).

We contend that even if eddies may have important local effects in modulating the stratification response and the exchange rates across the Taylor Cap's boundary, they likely do not control the overall structure of the Cap. This is based on the fact that we obtained similar results for our simulations when employing a standard eddy parameterisation (GM+Redi (Gent and Mcwilliams 1990; Redi 1982), results not shown). Our chosen resolution generates a Taylor Cap that resembles the observed one, and is thus deemed sufficient for understanding of the relative roles of barotropic vs. baroclinic dynamics. We relate this relative insensitivity to eddies to our conclusion that the baroclinic component does not play a leading role in the dynamics of the Taylor Cap at Maud Rise.

As a further check, we re-ran the case C2[-0.10] with a refined horizontal resolution of 5 km. For this case, the first baroclinic Rossby radius was ~ 12 km, indicating that this simulation was eddy permitting. Results are shown in Figure 8. Increasing the resolution leads to a finer structure in the SSH field, with an increased feature at the northeastern flank of the Gaussian bump, while the barotropic vorticity ζ_{bt} remains similar between resolutions. At depth, the distributions of temperature and vertical velocities are comparable as well. This strongly suggests that our conclusions drawn from the coarse-resolution experiments remain valid at higher resolutions, although even more resolution would be required to fully resolve eddies in this region.

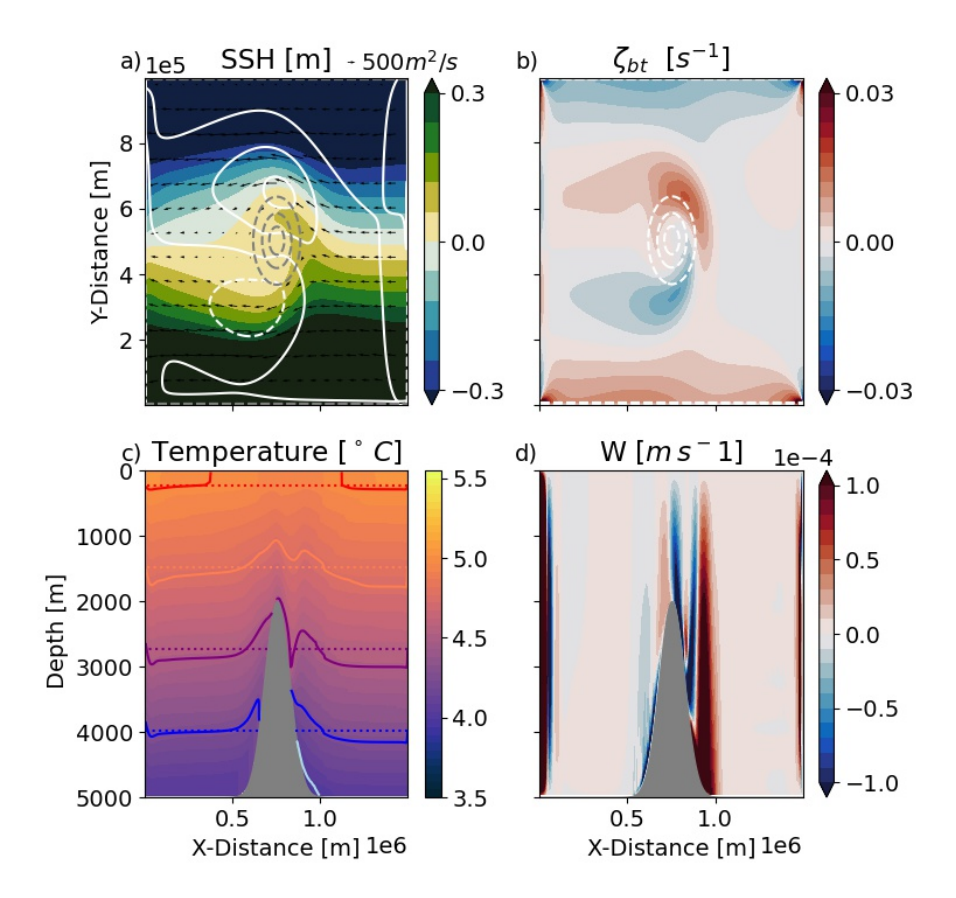


Fig. 8. Results of case C2 with a horizontal resolution of dx = dy = 5 km. a) SSH at the last output, with SSH anomalies and barotropic velocities (compare with Figure 3c). b) barotropic vorticity at the last output (compare with Figure 5d). c) Zonal temperature distribution, and d) vertical velocity section across the center of the bump at the last output (compare with Figures 6f-g).

This study has focused on the impact of the barotropic and baroclinic flows impinging on a topographic obstacle in the formation of a Taylor Cap and in the stratification's response, with relevance to Taylor Cap dynamics at Maud Rise. Our findings indicate that the Taylor Cap over the Rise is sensitive to the barotropic flow of the Weddell Gyre. The section used for creating cases E1 and E2 revealed a barotropic component that is approximately 10 times larger than its baroclinic counterpart. An intensified Weddell Gyre will lead to a stronger Taylor Cap and, concurrently, reduce upper-ocean stratification. The local forcing, e.g. surface atmospheric forcing or brine rejection during sea-ice production, sets the baroclinic component, which amplifies the response of stratification. In terms of the observed near-vanishing of Taylor Cap properties in 2014 in Gülk et al. (2023), this may suggest that the Weddell Gyre slowed down, and that thereby the barotropic flow must have been weakened at this time. An enhanced Weddell Gyre, on the other hand, should lead to a stronger Taylor Cap and reduced stratification at Maud Rise. Further, if the local forcing drives an increase in the stratification and, along with it, the baroclinic component of the flow, then the Taylor Cap could reach the upper-ocean mixed layer and trigger deep convection and the opening of a polynya.

In summary, the barotropic flow of the Weddell Gyre has been found to set the properties of the Taylor Cap at Maud Rise, and the baroclinic flow to modulate the internal structure of the water column. This suggests a large role for wind forcing in setting the properties of the Taylor Cap at Maud Rise via the barotropic flow of the wind-driven Weddell Gyre. As the Weddell Gyre interacts with the topography of Maud Rise, this interaction leads to a weakening of the stratification around Maud Rise by doming the isopyncals separating surface and subsurface layers. This work suggests that wind forcing therefore plays a large role in preconditioning the region of Maud Rise ahead of polynya event, in line with previous literature (Cheon and Gordon 2019).

This study also shows that triggering deep convection at Maud Rise requires more than solely varying the velocity of the impinging barotropic flow, as the stratification must also be weak enough to cross the convective threshold. This makes our work complementary to that of Alverson and Owens (1996), who investigated the impact of surface forcing on deep convection at Maud

Rise without consideration for the baroclinic nature of the impinging flow. The surface forcing anomalies do not have to be locally generated. In fact, the Weddell Gyre is known to advect buoyancy anomalies in form of salinity and temperature into the Maud Rise area (Kurtakoti et al. 2018; Gülk et al. 2023), and these variations impact the convective behaviour of the Taylor Cap and may eventually lead to the opening of a polynya (Narayanan et al. 2024). This issue of combining non-local surface forcing with a fully 3D ocean flow sensitive to strong bottom-flow interaction at Maud Rise remains to be explored to fully understand the conditions required for polynya opening.

- ⁵³⁸ Acknowledgments. BG, FR, DF and ACNG acknowledge support from the European Union's
- Horizon 2020 research and innovation programme under Grant Agreement No. 821001 (SO-
- ⁵⁴⁰ CHIC). The computations were enabled by resources provided by the National Academic In-
- frastructure for Supercomputing in Sweden (NAISS) and the Swedish National Infrastructure for
- 542 Computing (SNIC) at NSC partially funded by the Swedish Research Council through Grant
- ⁵⁴³ Agreement No. 2022-06725 and 2018-05973.
- Data availability statement. The set up and parameters of the idealized model configuration used
- to generate the model output and computer code to reproduce the plotted figures are available on
- 546 GitHub at https://github.com/bguelk/Taylor_Column. The SO-CHIC CTD data used for
- Figure 2e can be found at https://doi.org/10.17882/95314.

548 References

- Alverson, K., and W. B. Owens, 1996: Topographic preconditioning of open-ocean deep convection. *Journal of physical oceanography*, **26** (**10**), 2196–2213.
- ⁵⁵¹ Campbell, E. C., E. A. Wilson, G. K. Moore, S. C. Riser, C. E. Brayton, M. R. Mazloff, and L. D.
- Talley, 2019: Antarctic offshore polynyas linked to southern hemisphere climate anomalies.
- 553 *Nature*, **570** (**7761**), 319–325.
- Chapman, D. C., and D. B. Haidvogel, 1992: Formation of taylor caps over a tall isolated seamount in a stratified ocean. *Geophysical & Astrophysical Fluid Dynamics*, **64** (**1-4**), 31–65.
- Cheon, W. G., and A. L. Gordon, 2019: Open-ocean polynyas and deep convection in the southern ocean. *Scientific reports*, **9** (1), 1–9.
- De Steur, L., D. Holland, R. Muench, and M. G. McPhee, 2007: The warm-water "halo" around maud rise: Properties, dynamics and impact. *Deep Sea Research Part I: Oceanographic Research Papers*, **54** (6), 871–896.
- Francis, D., C. Eayrs, J. Cuesta, and D. Holland, 2019: Polar cyclones at the origin of the reoccurrence of the maud rise polynya in austral winter 2017. *Journal of Geophysical Research:*Atmospheres, **124** (**10**), 5251–5267.

- Gent, P. R., and J. C. Mcwilliams, 1990: Isopycnal mixing in ocean circulation models. *Journal of Physical Oceanography*, **20** (1), 150–155.
- Gordon, A. L., 1982: Weddell deep water variability. *Journal of Marine Research*, **40**, 199–217.
- Gülk, B., F. Roquet, A. C. Naveira Garabato, R. Bourdallé-Badie, G. Madec, and H. Giordani,
- ⁵⁶⁸ 2024: Impacts of vertical convective mixing schemes and freshwater forcing on the 2016–2017
- maud rise polynya openings in a regional ocean simulation. Journal of Advances in Modeling
- *Earth Systems*, **16** (**5**), e2023MS004 106.
- Gülk, B., F. Roquet, A. C. Naveira Garabato, A. Narayanan, C. Rousset, and G. Madec, 2023:
- Variability and remote controls of the warm-water halo and taylor cap at maud rise. *Journal of*
- *Geophysical Research: Oceans*, e2022JC019517.
- Hallberg, R., 2013: Using a resolution function to regulate parameterizations of oceanic mesoscale eddy effects. *Ocean Modelling*, **72**, 92–103.
- Hogg, N. G., 1973: On the stratified taylor column. *Journal of Fluid Mechanics*, **58** (3), 517–537.
- Holland, D., 2001: Explaining the Weddell Polynya-a large ocean eddy shed at Maud Rise.
- Science, **292** (**5522**), 1697–1700.
- James, I., 1979: The forces due to geostrophic flow over shallow topography. *Geophysical & Astrophysical Fluid Dynamics*, **14** (1), 225–250.
- Jena, B., M. Ravichandran, and J. Turner, 2019: Recent reoccurrence of large open-ocean polynya on the maud rise seamount. *Geophysical Research Letters*, **46** (**8**), 4320–4329.
- Kurtakoti, P., M. Veneziani, A. Stössel, and W. Weijer, 2018: Preconditioning and formation of maud rise polynyas in a high-resolution earth system model. *Journal of Climate*, **31** (**23**), 9659–9678.
- Leach, H., V. Strass, and B. Cisewski, 2011: Modification by lateral mixing of the warm deep water entering the weddell sea in the maud rise region. *Ocean Dynamics*, **61** (1), 51–68.
- Lellouche, J.-M., and Coauthors, 2021: The copernicus global 1/12° oceanic and sea ice glorys12 reanalysis. *Frontiers in Earth Science*, **9**, https://doi.org/10.3389/feart.2021.698876.

- Marshall, J., C. Hill, L. Perelman, and A. Adcroft, 1997: Hydrostatic, quasi-hydrostatic, and nonhydrostatic ocean modeling. *Journal of Geophysical Research: Oceans*, **102** (**C3**), 5733–5752.
- McPhee, M. G., 2003: Is thermobaricity a major factor in southern ocean ventilation? *Antarctic Science*, **15** (**1**), 153–160.
- Mohrmann, M., S. Swart, and C. Heuzé, 2022: Observed mixing at the flanks of maud rise in the weddell sea. *Geophysical Research Letters*, **49** (**8**), e2022GL098 036.
- Muench, R., J. Morison, L. Padman, D. Martinson, P. Schlosser, B. Huber, and R. Hohmann, 2001:
 Maud rise revisited. *Journal of Geophysical Research: Oceans*, 106 (C2), 2423–2440.
- Narayanan, A., F. Roquet, S. T. Gille, B. Gülk, M. R. Mazloff, A. Silvano, and A. C. Naveira Garabato, 2024: Ekman-Driven Salt Transport as a Key Mechanism for Open-Ocean Polynya Formation at Maud Rise. *Science Advances*.
- Ou, H. W., 1991: Some effects of a seamount on oceanic flows. *Journal of physical oceanography*, 21 (12), 1835–1845.
- Peña-Molino, B., S. Rintoul, and M. Mazloff, 2014: Barotropic and baroclinic contributions to along-stream and across-stream transport in the a ntarctic c ircumpolar c urrent. *Journal of Geophysical Research: Oceans*, **119** (**11**), 8011–8028.
- Proudman, J., 1916: On the motion of solids in a liquid possessing vorticity. *Proceedings of the Royal Society of London. Series A, Containing Papers of a Mathematical and Physical Character*, 92 (642), 408–424.
- Redi, M. H., 1982: Oceanic isopycnal mixing by coordinate rotation. *Journal of Physical Oceanog*raphy, **12 (10)**, 1154–1158.
- Schröder, M., and E. Fahrbach, 1999: On the structure and the transport of the eastern weddell gyre. *Deep Sea Research Part II: Topical Studies in Oceanography*, **46** (**1-2**), 501–527.
- Taylor, G. I., 1923: Experiments on the motion of solid bodies in rotating fluids. *Proceedings*of the Royal Society of London. Series A, Containing Papers of a Mathematical and Physical
 Character, **104** (**725**), 213–218.

Wunsch, C., 1997: The vertical partition of oceanic horizontal kinetic energy. *Journal of Physical Oceanography*, **27 (8)**, 1770–1794.